First-order reversal curve analysis of a Nd-Fe-B sintered magnet with soft X-ray magnetic circular dichroism microscopy

doi: 10.1016/j.actamat.2018.09.053

First-order reversal curve analysis of a Nd-Fe-B sintered magnet with soft X-ray magnetic circular dichroism microscopy

Kazunori Miyazawa[1], Satoshi Okamoto[1,2], Takahiro Yomogita[1], Nobuaki Kikuchi[1], Osamu Kitakami[1], Kentaro Toyoki[2,3], David Billington[2,3], Yoshinori Kotani[3], Tetsuya Nakamura[2,3], Taisuke Sasaki[2], Tadakatsu Ohkubo[2], and Kazuhiro Hono[2]

[1] Institute of Multidisciplinary Research for Advanced Materials (IMRAM), Tohoku University, Sendai 980-8577, Japan

[2] Elements Strategy Initiative Center for Magnetic Materials (ESICMM), National Institute for Materials Science (NIMS), Tsukuba 305-0047, Japan

[3] Japan Synchrotron Radiation Research Institute (JASRI), Sayo 679-5198, Japan

Abstract

First-order reversal curve (FORC) diagram, which visualizes the variation of magnetic susceptibility on a field plane, has been applied to a Nd-Fe-B sintered magnet. The FORC diagram exhibits the characteristic behavior of two remarkable spots in low-field and high-field regions. The high-field FORC spot corresponds to the irreversible magnetization reversal at a coercive field, whereas the low-field FORC spot indicates the appearance of a large magnetic susceptibility state during the demagnetization process. Moreover, this low-field FORC spot becomes dominant at high temperature, accompanied by a significant reduction in coercivity. These results suggest that the low-field FORC spot has a strong correlation with the degradation of magnetic properties of a Nd-Fe-B sintered magnet. To clarify the actual magnetization reversal processes corresponding to these two FORC spots, soft X-ray magnetic circular dichroism (XMCD) microscopy observation was employed with similar field sequences of the FORC measurements. Consequently, the low-field FORC spot is mainly attributed to the domain wall motion in multi-domain grains, whereas the high-field FORC spot corresponds to the magnetization reversal of single-domain grains. These indicate that a FORC diagram is a powerful evaluation method for the magnetization reversal processes of permanent magnets.

1 Introduction

Nd-Fe-B magnets [1,2] are indispensable for the traction motors of electric/hybrid vehicles. For further improvement of the energy efficiency of traction motors, enhancement of the magnetic energy density of Nd-Fe-B magnets at a high-temperature range is crucial. To tackle this issue, it is essential to understand the magnetization reversal process of Nd-Fe-B magnets [3-7].

First-order reversal curve (FORC) analysis is one of the magnetization reversal analysis methods [8-13]. This has been applied to various magnetic materials [12-20], including Nd-Fe-B magnets [21-24]. FORC is a magnetization curve measured by increasing the magnetic field H from a certain reverse field H_r on a major demagnetization curve. Thus, numerous FORCs are sequentially acquired by varying H_r along the demagnetization curve, and consequently, the inside of the major hysteresis curve is filled with the FORCs. As the magnetization M on each FORC is a function of H and H_r, the FORC distribution ρ is defined as the second-order derivation of M with respect to H and H_r,

$$\rho\left(H,H_r\right)=-\frac{\partial}{\partial H_r}\left(\frac{\partial M}{\partial H}\right) \quad . \tag{1}$$

Subsequently, ρ is plotted on the field plane with the axes of H and H_r. This plot is called as a FORC diagram. FORC analysis was originally proposed as an experimental approach to the Preisach model [8], which is the mathematical model of a hysteresis curve expressed by assuming an assembly of a reversal element, *i.e.*, hysteron, with distributions of coercivity and interaction field. Therefore, the FORC diagram is identical to the hysteron distribution if the magnetization reversal of the magnet follows the Preisach model. For this reason, FORC analysis has been expected to be an experimental evaluation method for coercivity and interaction field distributions.

However, the previously reported FORC diagrams of Nd-Fe-B sintered magnets are quite different from those expected from the Preisach model [21-23]. This fact means that the magnetization reversal process of Nd-Fe-B sintered magnets, which is considered as multiple events of nucleation, domain wall pinning, and domain wall propagation, is hard to be expressed as an assembly of a hysteron in the Preisach model.

Here, we elucidate the meaning of the FORC diagram pattern of Nd-Fe-B sintered magnets in a straightforward manner based on the definition of ρ. According to eq. (1), ρ is the variation of magnetic susceptibility ($\partial M/\partial H$) against H_r, and only irreversible magnetization reversal contributes to ρ. In this sense, a FORC diagram corresponds to the map of magnetic susceptibility variation presented on a field plane of (H, H_r). Therefore, detailed information on the magnetization reversal behavior is expected to be deduced by careful study of the FORC diagram pattern.

In this study, we have analyzed the FORC diagram pattern of a Nd-Fe-B sintered

magnet. Moreover, the relationship between the FORC diagram pattern and the actual magnetization reversal processes has been studied by means of high-spatial resolution magnetic domain observations using a soft X-ray magnetic circular dichroism (XMCD) microscopy.

2 Experimental

The magnet sample used in this study is a commercial standard anisotropic Nd-Fe-B sintered magnet with a chemical composition of $Fe_{76.0}Nd_{13.5}Pr_{0.2}Dy_{0.2}Tb_{0.2}B_{6.6}Cu_{0.1}Al_{0.5}Ni_{0.4}Co_{1.8}O_{0.5}$ in atomic ratio, and the microstructure of this magnet was elaborately analyzed in ref. [25]. FORCs were measured along the magnetic easy axis of the magnet at room temperature (RT) and 200 °C by using a vibrating sample magnetometer (VSM) with a maximum magnetic field of 2.6 T. To avoid the extrinsic deformation of magnetization curves owing to the demagnetization field [24], the magnet was shaped into a pillar of 3 mm in length and 0.5 mm in width, resulting in the demagnetization factor N_d of 0.04 along the long axis. The long axis of the pillar was set to be parallel to the magnetic easy axis of the magnet.

XMCD microscopy observation was performed at the soft X-ray beamline of BL25SU in SPring-8. The measurement temperature was RT. The sample was also shaped into a pillar of 10 mm in length and 0.5 mm in width, and the fresh surface of the Nd-Fe-B magnet for the XMCD measurement was obtained by fracturing it in a high vacuum condition (~3×10^{-6} Pa) of the sub-chamber of the XMCD measurement system. The fractured sample was immediately transferred into the main-chamber which is kept under an ultra-high vacuum condition (<5×10^{-7} Pa) [26,27]. The length of the fractured sample was approximately 7 mm, resulting in N_d of 0.011 along the long axis, which is almost comparable to that for the FORC measurements. The magnetic field was also applied along the long axis of the pillar using a superconducting magnet. The X-ray absorption signal was detected using a total electron yield (TEY) method at the Fe L_3 (707.9 eV) and Nd M_4 (1000.4 eV) edges. The X-ray beam with a diameter of approximately 100 nm was focused at the sample surface using a Fresnel zone plate, and the sample was scanned with a Piezo stage. Owing to the long focal depth (±5 μm) of this XMCD microscopy, the rugged fractured surface was directly observed without any surface-flattening processes [26, 27]. Significant deterioration of hard magnetic properties is usually observed in most magnetic imaging techniques, such as conventional magneto-optical Kerr microscopy and Lorentz transmission electron microscopy, owing to the surface defect introduced by mechanical polishing [28,29]. Therefore, the magnetization curves evaluated from these magnetic imaging methods exhibit much smaller coercivities than the original values of the samples. In contrast, the magnetization curve obtained from XMCD

using a sample fractured in an ultra-high vacuum is almost identical to that measured by VSM [30], indicating that the bulk magnetic property is maintained at the fractured surface. Fig. 1(a) shows an X-ray absorption image obtained at the Fe L_3 edge for the fractured surface of the Nd-Fe-B magnet. The morphological view of this image is similar to the scanning electron microscopy (SEM) image acquired from the same area, as shown in Fig. 1(d). Some grains in Fig. 1(a) exhibit maze-pattern contrast which is attributed to the different X-ray absorption depending on the magnetization direction. Most of the grains surface is covered with the thin Nd-rich phase since the grain-boundary Nd-rich phase is more fragile than the $Nd_2Fe_{14}B$ main phase [26,27,30]. Some grains, however, have the naked surfaces of the $Nd_2Fe_{14}B$ main phase due to the intra-grain fracturing. These inter-grain and intra-grain fractured regions are clearly distinguished by the chemical contrast mapping shown in Fig. 1(b), which is a differential image for the X-ray absorptions at the Fe L_3 and Nd M_4 edges. Since the TEY probing depth of the soft X-ray is about 1.2 nm [31], the chemical contrast is very sensitive to the surface chemical composition. Thus, the Nd- and Fe- rich regions can be assigned to the grains with inter-grain and intra-grain fracturing, respectively. The triple junctions and grain boundaries exhibit dark blue color, indicating that these are Nd-rich phases. In addition to these regions, many dark blue color spots are also found inside the grains. These are the Nd-oxide particles and/or fragments of triple junction at the grain surfaces. These spots are also visible as black ones in the X-ray absorption image obtained at the Fe L_3 edge in Fig.1(a).

The helicity of the X-ray is controlled using a system of twin-helical-undulator and kicker magnets. The XMCD image shown in Fig. 1(c) is obtained as a differential image of the X-ray absorptions with plus and minus helicities at the Fe L_3 edge. Very clear magnetic contrast can be obtained, and single-domain and multi-domain grains are clearly distinguishable [26,27]. The Nd-rich phases as mentioned above are represented as the gray color regions in the XMCD image.

3 Results and discussion

3.1 FORC measurements

Figs. 2(a) and 2(b) show the FORCs and the FORC diagram of the Nd-Fe-B sintered magnet measured at RT, respectively. From the major magnetization curve, the coercivity H_c is evaluated to be 1.2 T. In the FORC diagram (Figs. 2(b)), there are two remarkable spots around ($\mu_0 H$, $\mu_0 H_r$) = (0 T, −1.1 T) and (1.2 T, −1.5 T) highlighted by the red and blue circles, respectively. Hereafter, the former and latter are referred to as the low-field and high-field FORC spots, respectively. It is very interesting that these two FORC spots have been commonly observed in the previously reported FORC diagrams of Nd-Fe-B sintered magnets even though their

magnetic properties are different [21-23]. In these reports, the two FORC spots were simply explained as the existence of low-coercivity and high-coercivity regions, *i.e.*, the interpretations based on the Preisach model [8]. As mentioned in the introduction, however, such naïve explanation is not suitable for the FORC diagram of Nd-Fe-B sintered magnets. According to eq. (1), a FORC diagram is a visualization of the change in the magnetic susceptibility on a field plane of (H, H_r). Thus, the literal explanation for the low-field and high-field FORC spots based on eq. (1) is that there are two regions of large change in the magnetic susceptibility. It is apparent that the high-field FORC spot around ($\mu_0 H$, $\mu_0 H_r$) = (1.2 T, −1.5 T) corresponds to the large slope magnetization curves around the major curve coercivity encircled by the blue line in Fig. 2(a). The large slope magnetization curves corresponding to the low-field FORC spot is also observed around ($\mu_0 H$, $\mu_0 H_r$) = (0 T, −1.1 T), encircled by the red line in Fig. 2(a). Note that this large slope region corresponding to the low-field FORC spot in Fig. 2(a) disappears when H_r becomes negatively large enough. This behavior cannot be explained by the Preisach model. Moreover, another interesting point is the position of the high-field FORC spot, where is underneath the downward diagonal line of $H = -H_r$ in Fig. 2(b). If the high-field FORC spot locates on the line of $H = -H_r$, the coercivity H_c appears when H_r reaches the same amplitude of H_c. Therefore, the high-field FORC spot lying underneath the line of $H = -H_r$ indicates that the appearance of H_c requires the application of much larger field of H_r. From the position of the high-field FORC spot in Fig. 2(b), this magnet requires H_r of −1.5 T for the appearance of H_c of 1.2 T.

It should be mentioned that a small kink on the magnetization curve is observed at the remanence as encircled by the purple line in Fig. 2(a), indicating the presence of the surface-deteriorated magnetic layer due to the mechanical polishing [28,29]. One may say that this surface-deteriorated layer works as a detonator for the magnetization reversal of the whole magnet. The FORC diagram in Fig. 2(b), however, shows that the surface-deteriorated layer has a minor effect on the magnetization reversal of the whole magnet. As explained above, a FORC diagram pattern reflects only the irreversible magnetization reversal. The FORC spot pattern corresponding to the small kink is observed around ($\mu_0 H$, $\mu_0 H_r$) = (0 T, 0 T) on the FORC diagram in Fig. 2(b) (encircled by the purple line), but its contrast is very weak. This indicates that the surface-deteriorated layer causes a small amount of irreversible magnetization reversal in this magnet.

Figs. 3(a) and 3(b) show the FORCs and the FORC diagram of the Nd-Fe-B sintered magnet measured at 200 °C, respectively. Contrary to the results measured at RT shown in Fig. 2, the low-field FORC spot around ($\mu_0 H$, $\mu_0 H_r$) = (0 T, −0.1 T) becomes dominant. It is also confirmed that this very strong low-field FORC spot corresponds to the large slope regions of the magnetization curves highlighted by the red circle

in Fig. 3(a). On the other hand, the high-field FORC spot corresponding to H_c around ($\mu_0 H$, $\mu_0 H_r$) = (0.1 T, −0.3 T) encircled by the blue line in Fig. 3(b) is weak, and the deviation from the downward diagonal line of $H = -H_r$ becomes large. Note that the value of $\mu_0 H_r$ = −0.3 T for the position of the high-field FORC spot is close to the saturation field, indicating that the appearance of H_c at 200 °C requires almost the full saturation of the magnet.

3.2. XMCD microscopy

To understand the actual magnetization reversal processes corresponding to the low-field and high-field FORC spots on the FORC diagram of the Nd-Fe-B sintered magnet, the XMCD microscopy observation was performed for the fractured surface of the magnet.

Fig. 4 shows the XMCD magnetization curve and the XMCD images for the demagnetization process from the positive saturation. The XMCD magnetization curve (Fig. 4(a)) is obtained from the integrated XMCD signal. The magnetization curve by VSM is also plotted for comparison. These two magnetization curves are almost identical, indicating that the XMCD signal of the fractured surface well represents the magnetization of the whole magnet [26]. Figs. 4(b)-4(g) show the representative sequential XMCD images corresponding to the highlighted data points of the XMCD demagnetization curve in Fig. 4(a). The grains are rimmed by the black and white lines, which are the inter-grain and intra-grain fractured grains, respectively. Starting from the positive saturation at $\mu_0 H$ = 3 T, (Fig. 4(b)), multi-domain (MD) appears in some of the grains even near the remanence of $\mu_0 H$ = −0.3 T (Fig. 4(c)). The number of MD grains increases with decreasing H as shown in Fig. 4(d) at $\mu_0 H$ = −0.9 T. Note that these MD grains are in contact with each other, suggesting the presence of considerable inter-grain exchange coupling owing to the ferromagnetic grain-boundary phase [30,32-34]. With a further decrease in the magnetic field to $\mu_0 H$ = −1.5 T (Fig. 4(e)), the reversed regions expand to almost the entire area. However, some unreversed grains remain even at $\mu_0 H$ = −2.0 T (Fig. 4(f)). These unreversed grains are finally reversed at $\mu_0 H$ = −3.0 T (Fig. 4(g)).

Fig. 5 shows the XMCD magnetization curve and the XMCD images with the field sequence corresponding to the low-field FORC spot. The sample was first saturated at 3 T, and thereafter, the magnetic field was decreased to the reversal field $\mu_0 H_r$ = −1.0 T. Subsequently, the XMCD images were sequentially taken with increasing the magnetic field H. Although the reversal magnetization curve taken by XMCD somewhat deviates from that by VSM, the characteristic feature of the low-field FORC spot, which is the large slope at low H region, is clearly reproduced in the XMCD reversal magnetization curve, and the corresponding magnetization process is verified in the XMCD images. As discussed in Fig. 4, MD grains are observed during

the demagnetization process. These MD grains appear to be almost saturated at $\mu_0 H_r$ = −1.0 T (Fig. 5(b)), but some vestigial domains remain. These vestigial domains rapidly expand to MD state at $\mu_0 H$ = −0.3 T (Fig. 5(c)). The domain walls inside each grain easily move with slight increase in H, which is much smaller than the major curve coercivity (Figs. 5(d) and 5(e)). After the MD grains are almost saturated, some smaller grains remain in the single-domain (SD) reversed state (Figs. 5(f) and 5(g)). These SD grains gradually reverse with further increase in H.

Fig. 6 shows the XMCD magnetization curve and the XMCD images with the field sequence corresponding to the high-field FORC spot. In this case, the reversal field is $\mu_0 H_r$ = −1.5 T. Similar to the cases of the demagnetization curve and the low-field FORC spot shown in Figs. 4 and 5, the XMCD reversal magnetization curve for the high-field FORC spot is almost identical to that by VSM. On the other hand, the XMCD images exhibit different reversal behaviors compared with the case of the low-field FORC spot. The XMCD image at $\mu_0 H_r$ = −1.5 T (Fig. 6(b)) shows that most of the grains except for some smaller grains appear to be negatively saturated, and these negatively saturated grains are almost unchanged at $\mu_0 H$ = −0.5 T (Fig. 6(c)). This result indicates that the vestigial domains remaining at $\mu_0 H_r$ = −1.0 T, as discussed above, are collapsed at $\mu_0 H_r$ = −1.5 T. With a further increase in the magnetic field to $\mu_0 H$ = 0.6 T (Fig. 6(d)), some MD grains are observed similar to the case of the low-field FORC spot. After these MD grains are almost saturated, the SD grains gradually reverse with a further increase in H (Figs. 6(e) and 6(f)). The number of SD grains for the high-field FORC spot is apparently higher than that for the low-field FORC spot.

Fig. 7(a) shows the histogram of the ratio of MD reversed, SD reversed, and unreversed grain numbers as a function of the reversal field H_r. Figs. 7(b)-7(f) show the distribution map of MD and SD reversed grains for each H_r. It is evident that the MD reversal process is dominant in H_r in the first half of the demagnetization curve. On the other hand, the SD reversal process becomes dominant in H_r in the latter half of the demagnetization curve. Although there are many exceptions, a smaller grain with diameter less than 10 μm tends to undergo SD reversal. Probably, these MD and SD reversals depend not only on the grain size itself but also on the environmental condition of each grain such as the local magnetic properties of grain-boundary phase, local demagnetization field, and so on. Here, we do not observe a noticeable difference in the reversal processes between the inter-grain and intra-grain fractured grains.

3.3 Discussion

Let us discuss the relationship between the FORC diagram pattern of the Nd-Fe-B sintered magnet and the actual magnetization reversal processes. The FORC diagram

pattern of the Nd-Fe-B sintered magnet mainly consists of the low-field and high-field FORC spots, which correspond to the large slope reversal curves at the low-field and coercivity regions, respectively. Moreover, the high-field FORC spot is located underneath the downward diagonal line of $H = -H_r$. From the XMCD microscopy images sequentially taken with the similar field sequences for the low-field and high-field FORC spots, the large magnetic susceptibility for the low-field FORC spot is attributed to the domain wall displacement in each MD grain, which is preferentially formed in the first-half part of the demagnetization process. On the other hand, the high-field FORC spot is mainly attributed to the magnetization reversal of SD grains. From these results, it is understood that the high-field FORC spot appears after the firstly formed MD grains are fully saturated. Then, the position of the high-field FORC spot underneath the downward diagonal line of $H = -H_r$ represents the required field amplitude to fully saturate the MD grains.

Although the contrast of the high-field FORC spot is much stronger than that of the low-field FORC spot at RT, this relation becomes inverse at high temperature. This fact suggests that the significant degradation of the hard-magnetic properties of the Nd-Fe-B sintered magnet at high temperature is accompanied by the change in the dominant magnetization reversal process from the SD reversal to MD reversal. This picture is also applicable to the FORC diagram of Nd-Fe-B hot-deformed magnets, which exhibit only the high-field FORC spot even at elevated temperature [24]. Nd-Fe-B hot-deformed magnets consist of well-aligned thin platelet grains, and all the grains behave as the SD state during the magnetization reversal due to their very small grain size. Therefore, the magnetization reversal process of the Nd-Fe-B hot-deformed magnet does not change with temperature. This may be one of the reasons that Nd-Fe-B hot-deformed magnets generally exhibit good hard-magnetic properties at high temperature compared with Nd-Fe-B sintered magnets [35,36].

4 Summary

We studied the FORC analysis of a commercial Nd-Fe-B sintered magnet and its relationship with the actual magnetization reversal processes using XMCD microscopy.

We observed two FORC spots at low-field and high-field regions in the FORC diagram, which have been commonly observed in the previously reported FORC diagrams of Nd-Fe-B sintered magnets. The high-field FORC spot is dominant at ambient temperature, but the low-field one becomes dominant at 200 °C. Moreover, the high-field FORC spot is located underneath the downward diagonal line, indicating that the appearance of coercivity requires the application of sufficiently large demagnetizing field. From the XMCD microscopy measurements with similar field sequences of low-field and high-field FORC spots, these two FORC spots are

mainly attributed to the multi-domain and single-domain reversed grains, respectively. Therefore, the change in the contrast of the low-field and high-field FORC spots with temperature indicates the change in the dominant magnetization reversal process. Moreover, the position of the high-field FORC spot underneath the downward diagonal line represents the field amplitude required to saturate the firstly formed multi-domain grains.

Our results clearly demonstrate that the FORC analysis, which teaches us where and how magnetization reversal occurs on a field plane, is a powerful method to diagnose permanent magnets.

Acknowledgments

We gratefully thank Dr. S. Hirosawa for valuable advice and fruitful discussion. This work was partially supported by Dynamic Alliance for Open Innovation Bridging Human, Environment and Materials from MEXT, the Management Expenses Grants for National Universities Corporations from MEXT, JSPS KAKENHI Grant No. 17H03376, JST, Collaborative Research Based on Industrial Demand, and NIMS Joint Research Hub Program. The XMCD microscopy experiments have been performed at SPring-8 with the approval of JASRI (Proposal Nos. 2015A2042, 2015B1998, 2017A1022, and 2017B1028).

References

1 M. Sagawa, S. Fujimura, N. Togawa, H. Yamamoto, and Y. Matsuura, New material for permanent magnets on a base of Nd and Fe, J. Appl. Phys. 55 (1984) 2083-2087.

2 J. J. Croat, J. F. Herbst, R. W. Lee, and F. E. Pinkerton, High-energy product Nd-Fe-B permanent magnets, Appl. Phys. Lett. 44 (1984) 148-149.

3 K.-D. Durst and H. Kronmüller, The coercive field of sintered and melt-spun NdFeB magnets, J. Magn. Magn. Mater. **68** (1987) 63.

4 X. C. Kou, H. Kronmüller, D. Givord, and M. F. Rossignol, Coercivity mechanism of sintered $Pr_{17}Fe_{75}B_8$ and $Pr_{17}Fe_{53}B_{30}$ permanent magnets, Phys. Rev. B **50** (1994) 3849.

5 D. Givord, M. Rossignol, and V. Barthem, The physics of coercivity, J. Magn. Magn. Mater. **258–259** (2003) 1-5.

6 K. Kobayashi, K. Urushibata, Y. Une, and M. Sagawa, The origin of coercivity enhancement in newly prepared high coercivity Dy-free Nd-Fe-B sintered magnets, J. Appl. Phys. **113** (2013) 163910.

7 S. Okamoto, R. Goto, N. Kikuchi, O. Kitakami, T. Akiya, H. Sepehri-Amin, T. Ohkubo, K. Hono, K. Hioki, and A. Hattori, Temperature-dependent magnetization reversal process and coercivity mechanism in Nd-Fe-B hot-deformed magnets, J. Appl. Phys. **118** (2015) 223903.

8 I.D. Mayergoyz, Mathematical models of hysteresis, IEEE Trans. Magn. **MAG-22** (1986) 603-608.

9 C.R. Pike, A.P. Roberts, M.J. Dekkers, K.L. Verosub, An investigation of multi-domain hysteresis mechanisms using FORC diagrams, Phys. Earth Planet. Int. **126** (2001) 11–25.

10 A. Stancu, C. Pike, L. Stoleriu, P. Postolache, and D. Cimpoesu, Micromagnetic and Preisach analysis of the First Order Reversal Curves (FORC) diagram, J. Appl. Phys. **93** (2003) 6620-6622.

11 R. J. Harrison and J. M. Feinberg, FORCinel: An improved algorithm for calculating first-order reversal curve distributions using locally weighted regression smoothing, Geochem. Geophys. Geosyst. **9** (2008) Q05016.

12 C.R. Pike, A.P. Roberts, and K.L. Verosub, Characterizing interactions in fine magnetic particle systems using first order reversal curves, J. Appl. Phys. **85** (1999) 6660-6667.

13 D. A. Gilbert, G.T. Zimanyi, R.K. Dumas, M. Winklhofer, A. Gomez, N. Eibagi, J. L. Vicent, and K. Liu, Quantitative decoding of interactions in tunable nanomagnet arrays using first order reversal curves, Sci. Rep. **4** (2014) 4204.

14 J.E. Davies, O. Hellwig, E.E. Fullerton, G. Denbeaux, J.B. Kortright, and K. Liu, Magnetization reversal of Co/Pt multilayers: Microscopic origin of high-field magnetic irreversibility, Phys. Rev. B **70** (2004) 224434.

15 J.E. Davies, O. Hellwig, E.E. Fullerton, J.S. Jiang, S.D. Bader, G.T. Zimányi, and K. Liu, Anisotropy dependence of irreversible switching in Fe/SmCo and FeNi/FePt exchange spring magnet films, Appl. Phys. Lett. **86** (2005) 262503.

16 C.R. Pike, C.A. Ross, R.T. Scalettar, and G. Zimanyi, First-order reversal curve diagram analysis of a perpendicular nickel nanopillar array, Phy. Rev. B **71** (2005) 134407.

17 J. Yin, H. Zhang, F. Hu, B. Shen, and L.Q. Pan, First order reversal curve diagrams of perpendicular magnetic anisotropy films, J. Appl. Phys. **106** (2009) 103901.

18 V. Bonanni, Y. Fang, R.K. Dumas, C. Zha, S. Bonetti, J. Nogués, and J. Åkerman, First-order reversal curve analysis of graded anisotropy FePtCu films, Appl. Phys. Lett. **97** (2010) 202501.

19 N. Sakuma, T. Ohshima, T. Shoji, Y. Suzuki, R. Sato, A. Wachi, A. Kato, Y. Kawai, A. Manabe, and T. Teranishi, Exchange Coupling Interaction in $L1_0$-FePd/α-Fe Nanocomposite Magnets with Large Maximum Energy Products, ACS Nano **5** (2011) 2806-2814.

20 C.B. Rong, Y. Zhang, M.J. Kramer, and J.P. Liu, Correlation between microstructure and first-order magnetization reversal in the $SmCo_5$/α-Fe nanocomposite magnets, Phys. Lett. A **375** (2011) 1329-1332.

21 H. Chiriac, N. Lupu, L. Stoleriu, P. Postolache, and A. Stancu, Experimental and micromagnetic first-order reversal curves analysis in NdFeB-based bulk "exchange spring"-type permanent magnets, J. Magn. Magn. Mater. **316** (2007) 177-180.

22 T. Schrefl, T. Shoji, M. Winklhofer, H. Oezelt, M. Yano, and G. Zimanyi, First order reversal curve studies of permanent magnets, J. Appl. Phys. **111** (2012) 07A728.

23 P.A. Chen, C.Y. Yang, S.J. Chang, M.H. Lee, N.K. Tang, S.C. Yen, and Y.C. Tseng, Soft and hard natures of $Nd_2Fe_{14}B$ permanent magnet explored by first-order-reversal-curves, J. Magn. Magn. Mater. **370** (2014) 45-53.

24 T. Yomogita, S. Okamoto, N. Kikuchi, O. Kitakami, H. Sepehri-Amin, T. Ohkubo, K. Hono, T. Akiya, K. Hioki, and A. Hattori, Temperature and field direction dependences of first-order reversal curve (FORC) diagrams of hot-deformed Nd-Fe-B magnets, J. Magn. Magn. Mater. **447** (2018) 110-115.

25 T.T. Sasaki, T. Ohkubo, and K. Hono, Structure and chemical compositions of the grain boundary phase in Nd-Fe-B sintered magnets, Acta Mater. **115** (2016) 269-277.

26 Y. Kotani, Y. Senba, K. Toyoki, D. Billington, H. Okazaki, A. Yasui, W. Ueno, H. Ohashi, S. Hirosawa, Y. Shiratsuchi, and T. Nakamura, Realization of a scanning soft X-ray microscope for magnetic imaging under high magnetic fields, J. Sync. Rad. **25** (2018) 1444-1449.

27 D. Billington, K. Toyoki, H. Okazaki, Y. Kotani, T Fukagawa, T Nishiuchi, S. Hirosawa, and T. Nakamura, Unmasking the interior magnetic domain structure and evolution in Nd-Fe-B sintered magnets through high-field magnetic imaging of the fractured surface, Phys. Rev. Mater. (in press)

28 T. Fukagawa and S. Hirosawa, Coercivity generation of surface $Nd_2Fe_{14}B$ grains and mechanism of fcc-phase formation at the Nd/$Nd_2Fe_{14}B$ interface in Nd-sputtered Nd–Fe–B sintered magnets, J. Appl. Phys. **104** (2008) 013911.

29 M. Soderžnik, H. Sepehri-Amin, T.T. Sasaki, T. Ohkubo, Y. Takada, T. Sato, Y. Kaneko, A. Kato, T. Schrefl, and K. Hono, Magnetization reversal of exchange-coupled and exchange-decoupled Nd-Fe-B magnets observed by magneto-optical Kerr effect microscopy, Acta Mater. **135** (2017) 68-76.

30 T. Nakamura, A. Yasui, Y. Kotani, T. Fukagawa, T. Nishiuchi, H. Iwai, T. Akiya, T. Ohkubo, Y. Gohda, K. Hono, and S. Hirosawa, Direct observation of ferromagnetism in grain boundary phase of Nd-Fe-B sintered magnet using soft x-ray magnetic circular dichroism, Appl. Phys. Lett. **105** (2014) 202404.

31 B. H. Frazer, B. Gilbert, B. R. Sonderegger, G. De Stasio, The probing depth of total electron yield in the sub-keV range: TEY-XAS and X-PEEM, Surf. Sci. **537** (2003) 161-167.

32 H. Sepehri-Amin, T. Ohkubo, T. Shima, and K. Hono, Grain boundary and interface chemistry of an Nd–Fe–B-based sintered magnet, Acta Mater. **60** (2012) 819-830.

33 T. Kohashi, K. Motai, T. Nishiuchi, and S. Hirosawa, Magnetism in grain-boundary phase of a NdFeB sintered magnet studied by spin-polarized scanning electron microscopy, Appl. Phys. Lett. **104** (2014) 232408.

34 Y. Murakami, T. Tanigaki, T.T. Sasaki, Y. Takeno, H.S. Park, T. Matsuda, T. Ohkubo, K. Hono, and D. Shindo, Magnetism of ultrathin intergranular boundary regions in Nd–Fe–B permanent magnets, Acta Mater. **71** (2014) 370-379.

35 H. Sepehri-Amin, T. Ohkubo, S. Nagashima, M. Yano, T. Shoji, A. Kato, T. Schrefl, and K. Hono, High-coercivity ultrafine-grained anisotropic Nd–Fe–B magnets processed by hot deformation and the Nd–Cu grain boundary diffusion process, Acta Mater. **61** (2013) 6622-6634.

36 K. Hioki, A. Hattori, and T. Iriyama, Development of Dy-Free hot-deformed Nd-Fe-B magnets by optimizing chemical composition and microstructure, J. Magn. Soc. Jpn. **38** (2014) 79-82.

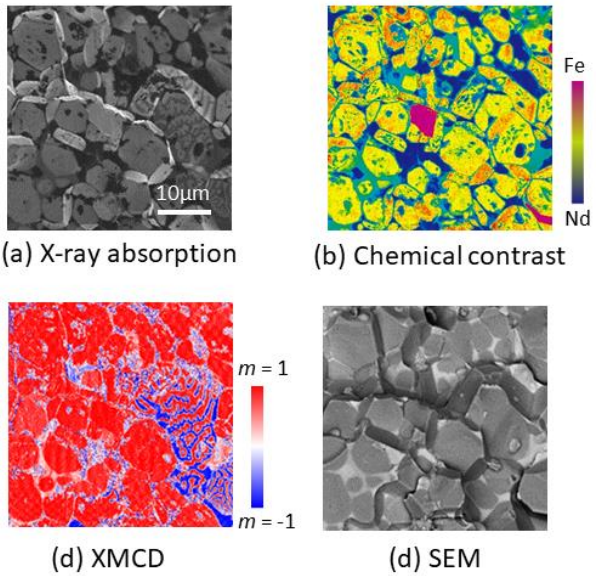

Figure 1 (a) X-ray absorption image at the Fe L_3 edge, (b) chemical contrast image of Fe and Nd taken by differential X-ray absorption at the Fe L_3 and Nd M_4 edges, (c) XMCD image at the Fe L_3 edge, and (d) SEM image of the fractured surface of the Nd-Fe-B sintered magnet taken for the same area of (a)-(c).

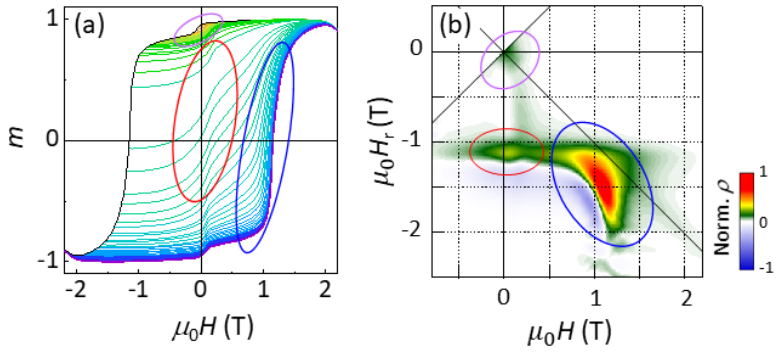

Figure 2 (a) FORCs and (b) FORC diagram of the Nd-Fe-B sintered magnet measured at RT. Color bar indicates the normalized value of ρ in the FORC diagram.

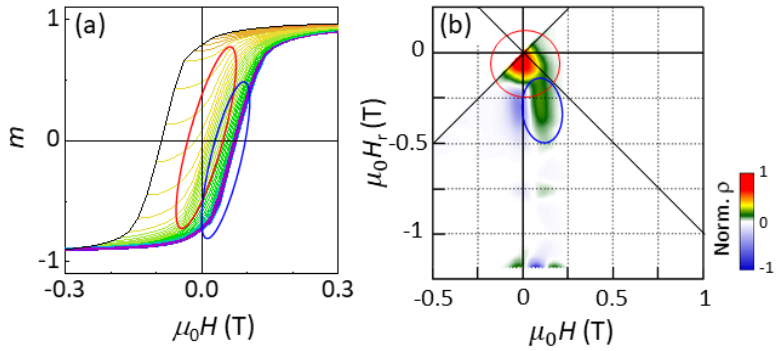

Figure 3 (a) FORCs and (b) FORC diagram of the Nd-Fe-B sintered magnet measured at 200 °C. Color bar indicates the normalized value of ρ in the FORC diagram.

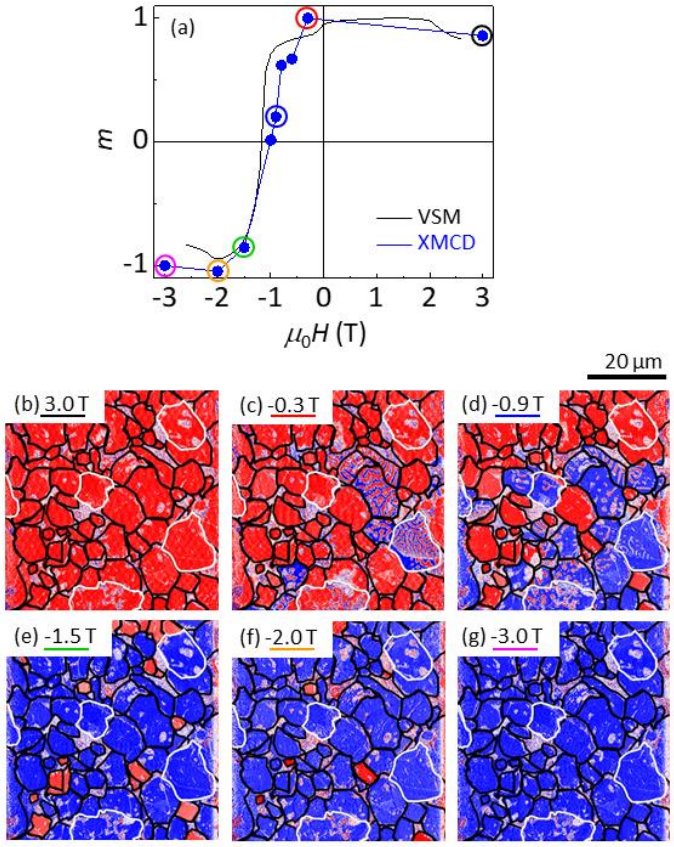

Figure 4 (a) XMCD demagnetization curve for the demagnetization process. The solid line is the magnetization curve by VSM. (b)~(g) XMCD images taken with the demagnetization field varying from 3 T to −3 T, corresponding to the highlighted data points in (a). The grains rimmed by black and white lines in (b)~(g) are the inter-grain and intra-grain fractured grains.

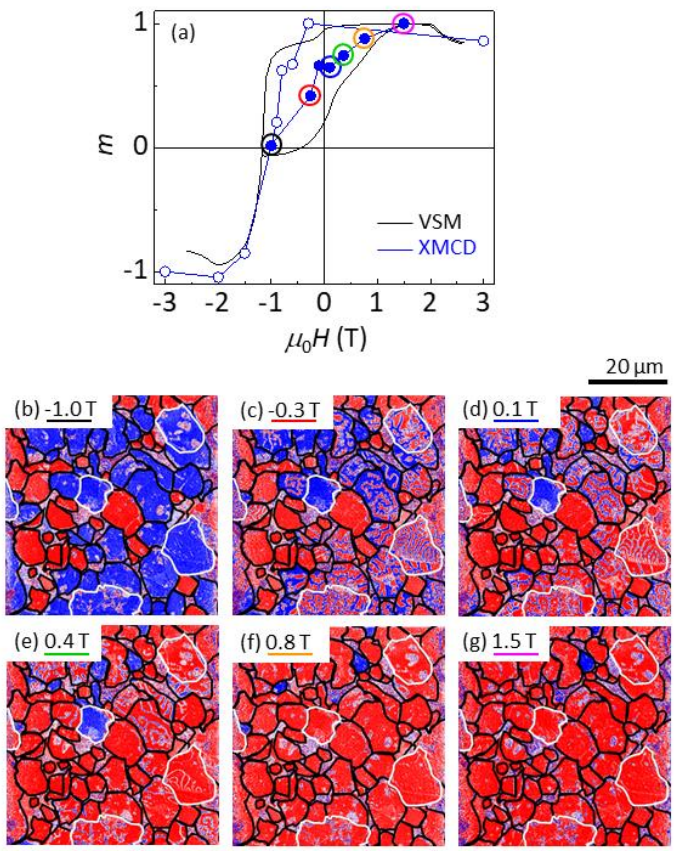

Figure 5 (a) XMCD reversal magnetization curve measured with similar field sequence of the low-field FORC spot ($\mu_0 H_r$ = −1 T). For comparisons, the XMCD demagnetization curve (open circles), and the VSM demagnetization and reversal curves (solid lines) are also plotted. (b)~(g) XMCD images taken with the field varying from −1 T to 1.5 T, corresponding to the highlighted data points in (a). The grains rimmed by black and white lines in (b)~(g) are the inter-grain and intra-grain fractured grains.

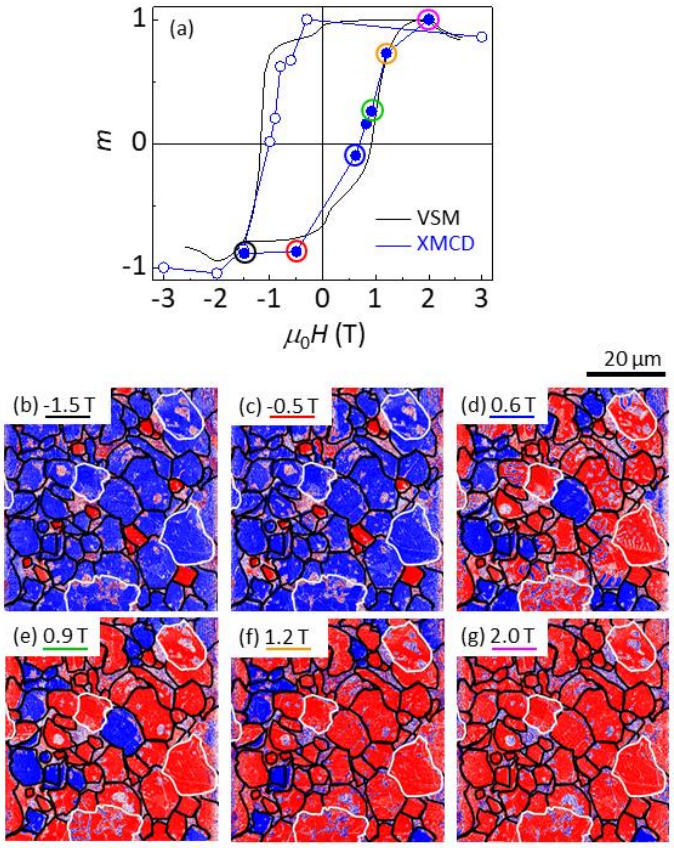

Figure 6 (a) XMCD reversal magnetization curve measured with similar field sequence of the high-field FORC spot ($\mu_0 H_r$ = −1.5 T). For comparisons, the XMCD demagnetization curve (open circles), and the VSM demagnetization and reversal curves (solid lines) are also plotted. (b)~(g) XMCD images taken with the field varying from −1.5 T to 2 T, corresponding to the highlighted data points in (a). The grains rimmed by black and white lines in (b)~(g) are the inter-grain and intra-grain fractured grains.

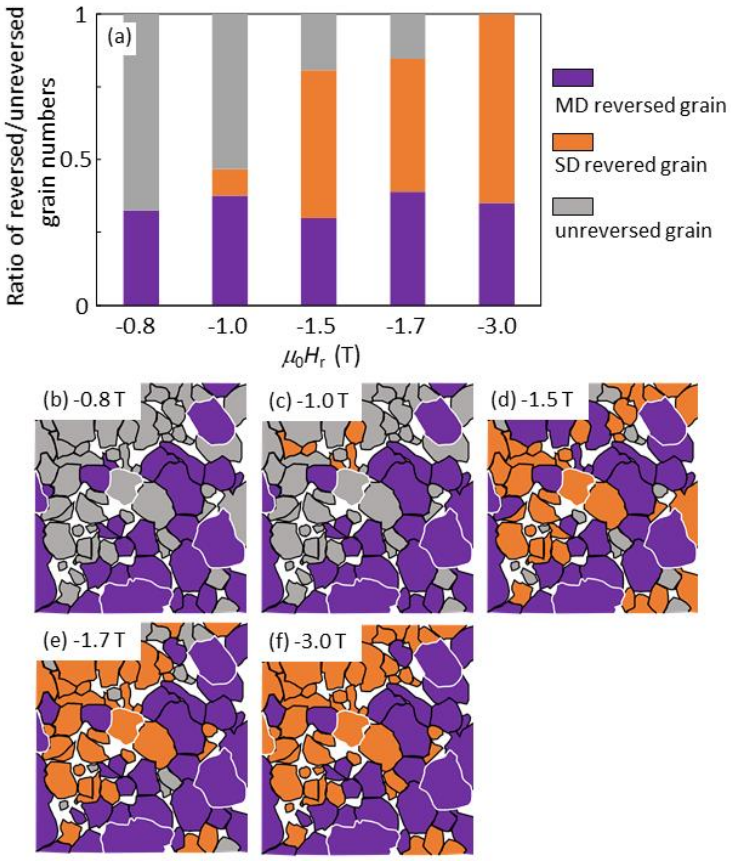

Figure 7 (a) Histogram of the ratio MD reversed, SD reversed, and unreversed grain numbers as a function of H_r. (b)~(f) Color maps of MD, SD, and unreversed grains at each H_r, corresponding to the data in (a). The grains rimmed by black and white lines in (b)~(f) are the inter-grain and intra-grain fractured grains.